SPECIALISED IMAGING

RESEARCH ARTICLE

Multi-frame multi-exposure shock wave imaging and pressure measurements

UK (Head Office / Factory)
6 Harvington Park,
Pitstone Green Business Park
Pitstone. LU7 9GX England
Tel **+44 (0) 1442 827728**

USA
Specialised Imaging Inc.
40935 County Center Dr. Suite D
Temecula, CA 92591, USA
Tel **+1 951-296-6406**

GERMANY
Hauptstr. 10,
82275 Emmering
Germany
Tel **+49 8141 666 89 50**

specialised-imaging.com **info@specialised-imaging.com**

bsi. ISO 9001:2015 Quality Management
FM 87429

Research Article | Vol. 30, No. 21 / 10 Oct 2022 / Optics Express 37664

Optics EXPRESS

Multi-frame multi-exposure shock wave imaging and pressure measurements

JAKA MUR,[1] FABIAN REUTER,[2] JERNEJ JAN KOČICA,[1] ŽIGA LOKAR,[1] JAKA PETELIN,[1] VID AGREŽ,[1] CLAUS-DIETER OHL,[2] AND ROK PETKOVŠEK[1,*]

[1]*Faculty of Mechanical Engineering, University of Ljubljana, Aškerčeva 6, SI-1000 Ljubljana, Slovenia*
[2]*Department Soft Matter, Faculty of Natural Sciences, Institute for Physics, Otto-von-Guericke University Magdeburg, 39106 Magdeburg, Germany*
[*]*rok.petkovsek@fs.uni-lj.si*

Abstract: Shock wave visual detection was traditionally performed using streak cameras, limited to homogeneous shock wave emission, with the corresponding shock wave pressure measurements available at rather large distances or numerically estimated through equation of state for water. We demonstrate a multi-frame multi-exposure shock wave velocity measurement technique for all in-plane directions of propagation, based on custom-built illumination system allowing multiple illumination pulses within each frame at multi-MHz frame rates and at up to 200 MHz illumination pulse repetition frequency at sub-nanosecond pulse durations. The measurements are combined and verified using a fiber-optic probe hydrophone, providing independent shock wave pressure and time-of-flight measurements, creating a novel all-optical measurement setup. The measured pressures at distances around 100 µm from the plasma center exceed 500 MPa, while camera-based measurements at even shorter distances indicate pressures above 1 GPa.

1. Introduction

A focused laser pulse in a liquid environment with sufficient intensity may vaporize the liquid, resulting in a localized explosive phase transition. The interaction of pulsed lasers with liquids is exploited in several contemporary applications, for example in eye surgery [1,2], wafer cleaning [3], tattoo removal [4], as an acoustic source [5], laser-induced breakdown spectroscopy in liquids [6], etc.

In general, when the laser intensity is below the dielectric breakdown threshold, the focal volume is heated up by linear absorption. That may result in superheating, leading to liquid-vapor phase change followed by a vapor bubble expansion. If the intensity in water is above the dielectric breakdown threshold intensity, for example, at about 70 GW/cm^2 for a pulsed laser with pulse duration of 6 ns at a wavelength of 1064 nm, non-linear absorption may instead result in the generation of a short lived plasma [7]. After free electron recombination, a hot vapor region is formed with approximately the same density as water [8]. Again, a rapidly expanding vapor bubble is nucleated, accompanied by shock wave emission. Within the first few nanoseconds, the expansion velocity of the vapor bubble is slowed down below the shock wave velocity, resulting in the detachment of a shock wave and its propagation through the undisturbed liquid. Only after the shock wave passage the liquid accelerates and the common simple bubble expansion models based on an incompressible liquid flow can be applied [9].

To measure the velocity of the shock wave, several techniques have been developed over time. All rely on a common principle that the shock wave in liquid becomes visible as a phase object as the pressure modulates the index of refraction [10]. This property was early on utilized in a sensitive light gate setup, where fast photo detectors probe the light intensity of two optical paths, which the shock wave crosses. This results in a modulation of the light intensity [11]. The

#470695 https://doi.org/10.1364/OE.470695
Journal © 2022 Received 20 Jul 2022; revised 9 Sep 2022; accepted 13 Sep 2022; published 27 Sep 2022

Optics EXPRESS

shock wave velocity can be obtained from the known distance and the measured time. A second method relies on the repeatability of the laser pulses and other laser-induced breakdown (LIB) conditions. In this case single images of the shock front with a short exposure allow depicting the front as a function of the delay between laser and image exposure [12]. Planar imaging has the advantage that non-isotropic propagation of the shock front can be properly accounted for. Exposing the image twice with a precise delay between the illumination pulses allows to determine the pressure of complex and non-repeatable shock wave fronts [13]. If only a specific propagation direction is of interest, then a streak image recording is a very elegant method to measure the shock wave velocity [14] as a function of the distance from the vapor bubble. The streak principle has been widely used in cavitation research [14–16] and is characterized by imaging an input slit on a screen while the image is swept in orthogonal direction with respect to the slit direction at a constant and well-known speed, allowing precise but only one-dimensional shock wave propagation measurements. The modulation of the index of refraction is also utilized in the background oriented Schlieren method [17] and high-speed shadowgraph imaging [18]. Here the deformation of a pattern imaged through the shock wave is obtained from an optical flow algorithm and the Gladstone–Dale relationship between pressure and index of refraction [19]. Alternative methods, such as time-stretch dispersive Fourier transformation, also exist [20].

An important observable of the liquid-laser interaction is the pressure of the shock front [21]. Here, optical measurements have proven an invaluable tool due to their non-invasiveness and their ability to measure very close the vapor phase. Most optical techniques are based on the jump condition across the shock front, which relates the shock wave velocity u_s with the particle velocity u_p: $p_s - p_0 = u_s u_p \rho_0$, where ρ_0 and p_0 are the density and the pressure ahead of the shock and p_s the shock wave pressure. The missing relationship between the particle velocity u_p and the shock velocity is provided by an equation of state. For sufficient low pressures, i.e. below 10 kbar, a linear relationship is valid for water, which holds for data obtained by Rice & Walsh [22]. However, for higher pressures of up to 250 kbar a non-linear function was found to represent the measured data, leading to a final relationship between the shock wave pressure and velocity:

$$p_s - p_0 = c_1 \rho_0 u_s 10^{\left(\frac{u_s - c_0}{c_2} - 1\right)}, \tag{1}$$

where constant velocities c_0, c_1, and c_2 are equal to 1500 m/s, 5190 m/s, and 25306 m/s, respectively [15]. Traditionally, corresponding shock wave pressure measurements are only available at rather large distances from the LIB center [11,18,21,23–25] or are estimated numerically [26–28].

In the present work we combine the multi exposure technique with high-speed imaging, where each frame in the high-speed imaging series is multiple times exposed with a laser pulse much shorter than the frame exposure time. For further verification and comparison, we have used a custom designed high-bandwidth fiber-optic probe hydrophone (FOPH) [29], similar principle as [5], providing independent shock wave pressure and time-of-flight measurements. Shock wave pressure and velocity measurements were thus obtained at high spatial resolution, effectively increasing the framing speed of the utilized high-speed cameras up to 20-fold. The measurements provide a detailed insight into shock wave pressure evolution to below 100 µm distances from the plasma center, revealing transient pressure amplitudes of more than 500 MPa. The presented method surpasses the previously demonstrated multi-exposure methods by an order of magnitude [30,31]. The frame rate is increased by a factor of 50 and the pulse duration decreased by a similar factor compared to [30], allowing for burst illumination at MHz frame rates.

2. Experimental setup

We demonstrate the multi-frame multi-exposure technique in combination with two of the present state-of-the art digital high-speed framing cameras in two separate experimental setups. Both

Optics EXPRESS

setups accommodated a nanosecond excitation laser, microscopic imaging, and the custom-built ultra-fast illumination system. The second setup additionally incorporated the FOPH pressure sensor for comparison with the image-based pressure measurement and additional single-point time-of-flight shock wave velocity measurement. The experimental setup schematics and the timing diagram are shown in Fig. 1.

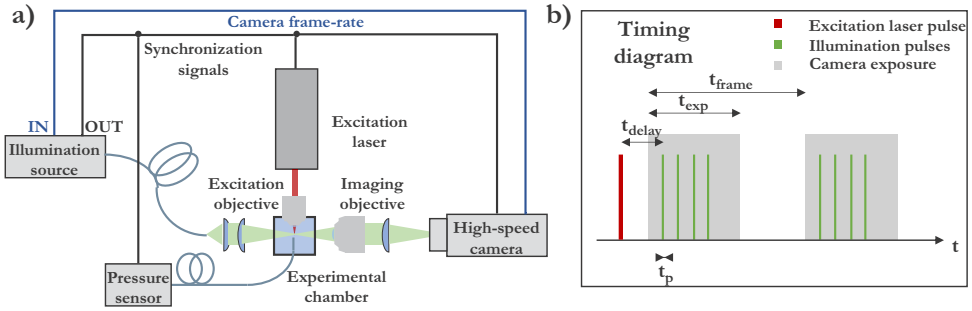

Fig. 1. a) Experimental setup schematic drawing, and b) timing diagram. Synchronization timing jitter between the excitation laser pulse and the camera exposure was approx. 1 ns, and well below 1 ns between the camera exposure signal and optical illumination pulses.

2.1. Illumination system

A custom-built short-pulse illumination system was used for imaging the cavitation bubble dynamics and the emitted shock wave. The illumination pulse bursts were delivered by a multimode fiber, and focused at the region of interest with a numerical aperture (NA) of 0.2. For the present study, we chose bursts consisting of four pulses with an individual pulse duration t_p of 0.3 ns at a central wavelength of 515 nm. The duration is sufficiently short to freeze the motion of the propagating shock wave. As a result, the shock wave is imaged four times within a frame of the high-speed camera. While the shock wave velocity is clearly separated due to the high propagation velocity, the expanding bubble with a 10-100 times smaller velocity is still imaged with a sharp boundary. The time delay between pulses in a burst was varied between 5 ns and 30 ns. Both cameras operated at 5 MHz, resulting in t_{frame} of 200 ns, t_{exp} around 100 ns, while the delay between excitation laser pulse and the first illumination pulse was varied (t_{delay}). The timing diagram is shown in Fig. 1(b).

The illumination system was locked to the camera's frame rate (Fig. 1(b), illumination pulses are in the same position with respect to exposure time t_{exp} and within each frame), while also providing precisely defined synchronization signals to the excitation laser and the trigger for the camera. The whole setup was phase-locked to the internal clock of the camera that resulted in jitter well below 1 ns for either electric or optical signals, which ensured repeatable imaging with sufficient precision in the time-domain. The timing delay between the excitation laser pulse and illumination pulses was thus well defined, as shown in Fig. 1(b). The shock wave position after an individual LIB event could be imaged at any given position, finally limited in precision only by the camera resolution. A typical set of images taken at different time delays is shown in Fig. 2, while the whole bubble evolution is shown in Fig. 3. Both sets are taken from Experimental setup 1.

2.2. FOPH

A fiber-optic probe hydrophone (FOPH) measured the transient shock wave pressure, which besides the pressure amplitude allowed to obtain the shock wave time-of-flight (TOF), i.e., the time delay between the excitation laser pulse and the shock wave front arrival on the FOPH fiber

Optics EXPRESS

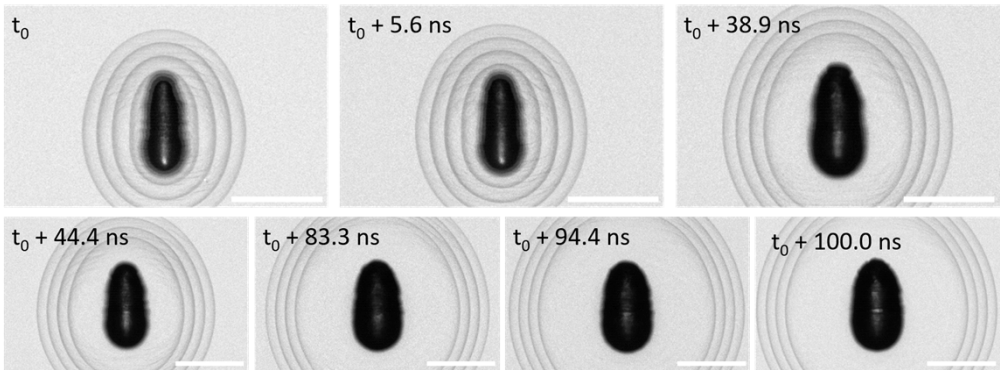

Fig. 2. Shock wave imaging with four pulse burst illumination at different time delays after the LIB event, showing 7 individual LIB events. The t_0 denotes the initial nonzero delay. Scale bars are equal to 200 µm.

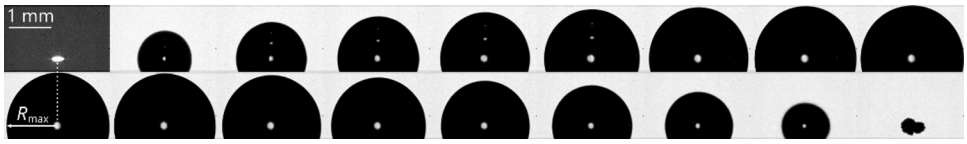

Fig. 3. Time series over the entire first oscillation cycle of the bubble developing from the plasma, the time between two frames is 10 µs, i.e. a span of 170 µs is covered in this series. The first image shows the plasma, and the background is presented darker for clarity. Only a section of the spherical bubble is shown.

tip. The FOPH was based on a single-mode fiber with 5.0 µm core diameter, 125 µm cladding diameter, and 6.6 µm mode field diameter as the sensing element. It delivered light at NIR (1.0 µm wavelength), resulting in 500-1000 mV steady state signal on the oscilloscope due to reflection at the tip. Further details are available in [29]. It was positioned perpendicular to the incident excitation laser beam direction and oriented with minimal tilt. The FOPH was mounted on a 3D positioning stage enabling accurate positioning. The reflected light from the FOPH tip was detected by a 5 GHz photodiode (Thorlabs DET08CFC), and the corresponding signal from the photodiode recorded with an oscilloscope (Agilent DSO81204B Infiniium; 12 GHz analog bandwidth). The TOF measurements had an unknown, but constant time delay added to the actual time delay due to different cable length, diode response times, etc. This was considered during the data processing by extracting the average slope from the data points by fitting a model function. For this, we used Eq. (1), an assumption of $p(r) \propto 1/r$, and the definition of velocity $u_s = dr/dt$. The obtained differential equation was then solved numerically to obtain the best fit parameters.

The working principle of the FOPH is based on the light reflectance at the glass–water interface of the submerged fiber tip. The light reflectance is a function of the refractive index, which is varying with time due to the water density modulation by the pressure wave, and the time varying intensity was detected by the photodiode. The resulting fast voltage change on the photodiode is then converted into pressure changes. The principle of conversion is based on the values of refractive index for water (1.32) and quartz (1.45) at standard conditions, and the Fresnel equations, the corresponding refractive index change Δn was calculated. The functional dependency of the refractive index of water n changing with pressure p has been obtained from the combined data on water density changing with pressure from NIST [32], ranging from 0. 1 MPa to 918 MPa, and the refractive index dependency on water density from [33], both presented

Optics EXPRESS

in Fig. 4(a). The Δn values were converted to pressure changes through the presented calibration curve, also considering 63 % reflected acoustic wave amplitude, giving the pressure sensor a valid range of actual pressures from 0.1 MPa to above 500 MPa, with the noise equivalent pressure in the range of 1 MPa. Sample pressure traces are shown in Fig. 3(b). Further details regarding the FOPH design and operation can be found in [29]. The FOPH positioning in respect to the initial LIB position is shown in Fig. 6(a).

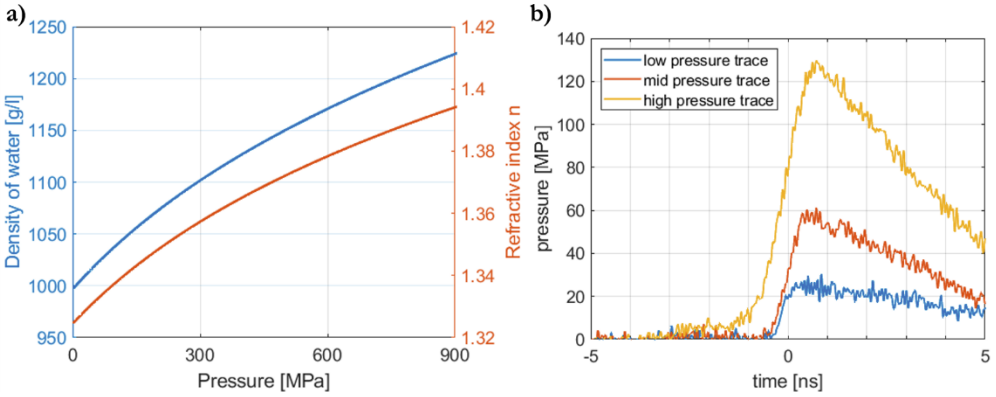

Fig. 4. a) Refractive index and density of water, plotted versus pressure, and b) sample pressure traces from the FOPH, showing shock wave arrival at 0 ns.

2.3. *Experimental setup 1 – excitation laser energy variation*

In the first experimental setup (Experiment 1), the LIB was generated using a green nanosecond laser, working at a 532 nm wavelength with the pulse duration of 6 ns (Litron Nano SG-100-2), coupled to a laboratory made 3D printed experimental chamber with illumination- and viewports made from cover glass. The excitation laser was focused with a Mitutoyo 50x objective with a numerical aperture of 0.42 and a nominal working distance of 20.5 mm in air. The laser energy was controlled by an external attenuator, with a maximum available energy of approx. 15 mJ, resulting in a maximum bubble radius $R_{max} = 1.35\ \text{mm} \pm 0.05\ \text{mm}$. The energy was parametrically tuned between 5 % and 100 % of the maximum laser energy. Plasma shape and size and initial bubble size were highly repeatable and the standard deviation of the bubble size for the same laser energy was below 2 % R_{max}. Only close to the optic breakdown threshold, here at 5 % and 10 %, sporadically the plasma was fragmented and the bubble of different shape. These measurements have been discarded from data evaluation.

Coupled to the illumination system, the Shimadzu Hyper Vision HPV-X2, high-speed camera set to a 5 MHz framing rate (resolution of 400×300 pixels) recorded the cavitation bubble and shock waves. The camera imaged the scene with a long-distance microscope objective with 10x magnification (Mitutoyo, NA of 0.3). The resulting magnification was 1.78 µm/pixel.

Another high-speed camera was used in perpendicular perspective. It was operated at a framing rate of 100 kHz with pixel resolution of 10.1 µm/px. It recorded the bubble dynamics over a longer time span, covering several oscillations and is used to measure the maximum bubble radius R_{max} which gives a measure for the amount of energy deposited via the laser, see below. An example is given in Fig. 3. The first frame shows the plasma, its center is taken as the centroid of bright pixels. Here only a section of the spherical bubble is shown, which is sufficient to measure the bubble radius as sketched. Consistent bubble sphericity was assured from further recordings covering the entire bubble at the price of lower temporal resolution due to pixel read-out rate limitations of the camera.

Optics EXPRESS

2.4. Experimental setup 2 – verification and pressure measurements

In the second experimental setup (Experiment 2), the LIB was generated with an infrared nanosecond excitation laser, working at a 1064 nm wavelength with the pulse duration of 5 ns, and an available energy of 15 mJ. The laser pulse was focused in water by a lens system with NA of 0.2, resulting in a maximum bubble radius $R_{max} = 1.67\ \text{mm} \pm 0.05\ \text{mm}$.

The illumination of the cavitation bubble and shock waves was again based on the custom-built short-pulsed illumination system, but combined with a different high-speed camera, namely the Specialised Imaging Kirana 7M operating at a 5 MHz framing rate (resolution of 924×768 pixels). The camera was used in combination with an imaging microscope objective with 10x magnification (OptoSigma, NA of 0.3). The resulting resolution was 3.47 µm/pixel on the final images. The combination of high frame rate, camera resolution, and optical magnification allowed us to image the shock wave propagation over multiple frames, using burst illumination on each subsequent frame (Fig. 5). Again, the pulse rate of the illumination system was locked to the camera frame rate while also providing synchronization signals for the remaining devices. In Experiment 2, the imaging was complemented by the additionally incorporated FOPH.

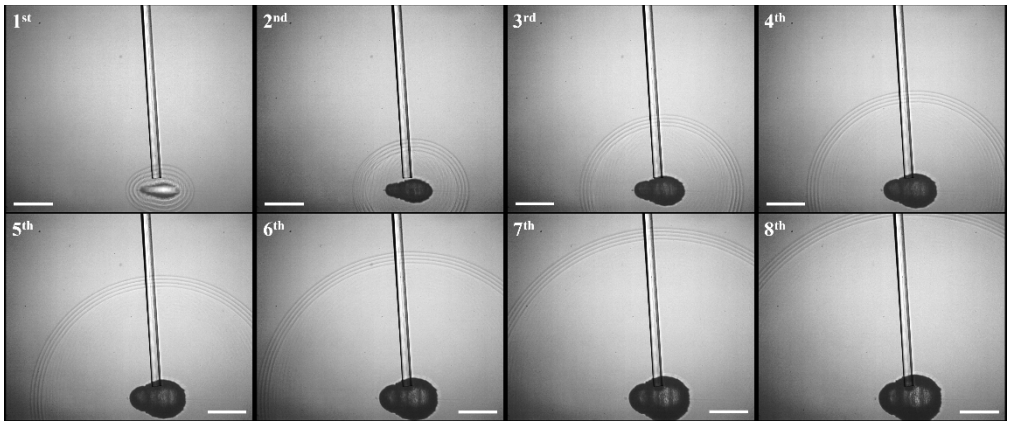

Fig. 5. Shock wave propagation following a single LIB event shown on 8 consecutive frames from the Kirana camera at 5 MHz, capturing the same shock wave at 32 different times due to burst illumination. The FOPH is visible in the images, providing a simultaneous shock wave pressure and time-of-flight measurement at its tip position. Scale bars equal to 500 µm.

2.5. Shock wave front recognition

Automatized shock wave front recognition from camera-based images was realized in Matlab, using peak detection functions. Third order 2D-polynomial interpolation was used to achieve sub-pixel accuracy together with spatial averaging through curve fitting along the shock wave front. This allowed a robust detection of the shock front, see Fig. 6(b), and we expect a wave front localization accuracy better than 0.3 pixel i.e. 0.6 µm and 1.1 µm, respectively for the two imaging systems. With the precisely known delays between the illumination pulses, the shock wave velocity was calculated as $u_s = (y_1\text{-}y_2)/\Delta t$, where y_1 and y_2 are two subsequent shock wave positions, and Δt is the time delay between subsequent illumination pulses. The shock wave velocity was the average velocity at a position $(y_1 + y_2)/2$ away from the plasma center along the short axes of the generated quasi-elliptical shock fronts, corresponding to the closest direction of shock wave propagation to the FOPH measurements (shown in Fig. 6(a)). The shape of the plasma and consequently of the initial bubble is characteristic to the laser and the focusing optics.

Optics EXPRESS

This becomes apparent from comparison of Fig. 6 and Fig. 2, which are generated in the two similar setups described in Section 2.3 and 2.4, respectively.

3. Results and discussion

The TOF measurements from the FOPH had to be converted into shock wave velocity for an independent comparison with camera-based velocity measurements. The conversion was done by numerical fitting of velocity evolution versus distance and checking its integral against the TOF data. The velocity evolution calculation was based on the pressure profile converted into velocity evolution using Eq. (1). The pressure profile was the starting point, and was assumed proportional to $1/r$, which is exact for a linear acoustic wave and thus at large distances, and a first approximation for finite acoustic waves closer to the LIB, see Ref. [34]. The agreement between this approximation and our pressure measurements is also presented in this work (inset of Fig. 9). Notably, related works of other groups show faster pressure decay with distance [35–37,27,34], but typically at shorter distances compared to this work. In short, the TOF model calculation was based on assuming the validity of Eq. (1) and the initial pressure profile, in the end providing a reasonable match to the measured data points (the end result is shown in Fig. 7(a)), with expected deviation at distances below 100 µm from the plasma center. The variation observed in the measured TOF data points is mostly the consequence of fiber tip positioning errors in respect to the plasma center position, with the simulated curve averaging out the measurement uncertainty.

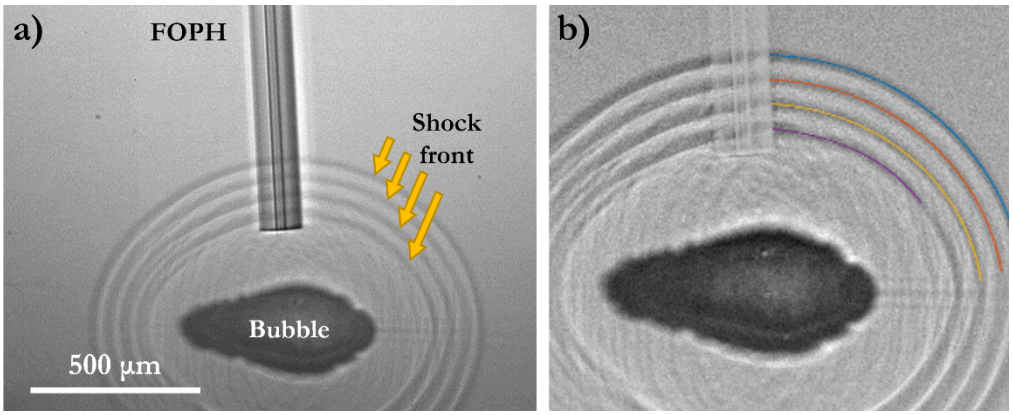

Fig. 6. a) Shock wave propagation near the initial LIB region and pressure sensor (FOPH) positioned nearby. The excitation laser pulse propagated from right to left. b) Improved contrast, background removed, and shock wave front recognition result. Different colors show the recognized position of the same shock wave front at different illumination times.

Shock wave velocity measurements from both experiments, based on the optical recognition of multiple shock wave front positions within the same camera frame (Experiment 1) and through multiple consequent frames (Experiment 2), are presented in Fig. 7(b)**.** In addition, the TOF-based velocity measurements from the FOPH are added to the same graph, being independent from the camera-based measurements and pressure measurements (the latter are shown in Fig. 9). Measurements start at approx. 100 µm from the plasma center and continue to about 400 µm for data from Experiment 1, and up to 2 mm in Experiment 2. At the largest distances, approximately corresponding to maximum bubble radius, the shock wave propagation velocity has already decayed very close to a value close to the speed of sound in water (1490 m/s ± 10 m/s) at $T = 22$ °C and $p_0 = 10^5$ Pa. The measurements from both experiments are in a good agreement, considering different maximal bubble radii and plasma shape, leading to differences in both the initial shock wave energy and shape, the latter being non-spherical.

Optics EXPRESS

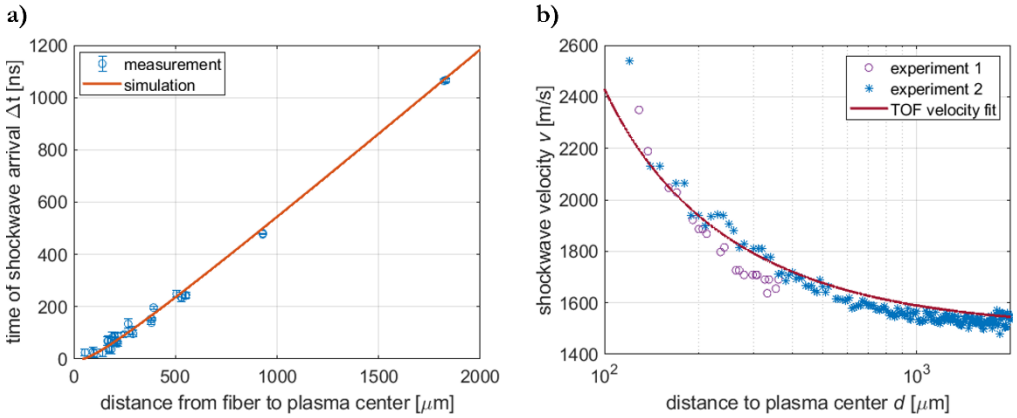

Fig. 7. a) Time-of-flight (TOF) measurement from pressure sensor with the corresponding velocity distribution integral, and b) shock wave velocity measurements from both experiments (camera-based) with the TOF velocity distribution plotted as a continuous line. Bubble sizes were maximal for both experiments, 1.35 mm and 1.67 mm, respectively.

Figure 8 depicts the shock velocity decay as a function of the distance from the plasma center for different excitation laser intensities. The laser intensity was varied between 5 % and 100 % in steps of 5 %, which resulted in maximal bubble radii ranging between 0.36 mm and 1.35 mm, i.e., exhibiting an approximately 50-times increase in bubble energy between the smallest and largest bubbles. According to Ref. [15], the acoustic energy emitted by the plasma shock wave is similar to the energy of the volumetric expansion work done by the expanding bubble $E_b = 4/3\pi R_{max}^3 p_0$, where $p_0 = 10^5$Pa is the atmospheric pressure and R_{max} was obtained from the high-speed images.

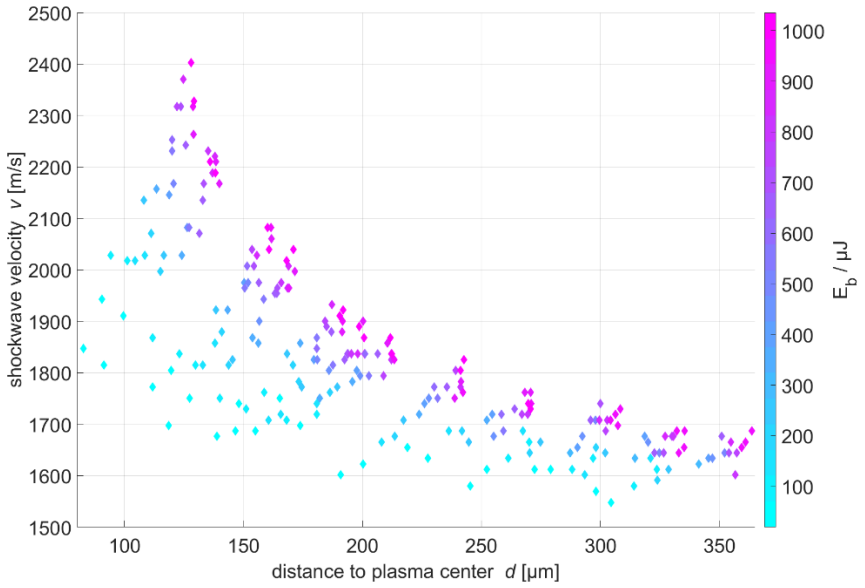

Fig. 8. Shock wave speed measurements for different excitation laser energies within Experiment 1, color coded for the corresponding bubble energy E_b.

Optics EXPRESS

Figure 8 reveals that all measurements in the presented range of distances are far above the linear speed of sound. Here the first measurement location at a distance of 80 µm is limited by the need that two consequent shock wave positions are imaged and separated from the plasma to measure the average velocity at that position. Figure 8 also demonstrates that with lower excitation laser energies, the shock wave velocity measurements consistently show a lower velocity at the same distances from the plasma center, compared to higher excitation laser energies. This agrees with theoretically expected lower pressures due to lower shock wave energies corresponding to lower excitation laser energies.

The inset of Fig. 9 depicts the measured pressure from the pressure sensor with a *1/r* fit for comparison taken from Experiment 2. These values are compared to the image-based measurements of both experiments. Therefore, the shock wave velocity measurements were converted into pressure values, using Eq. (1). The comparison of the two experiments with the pressure sensor are shown in Fig. 9.

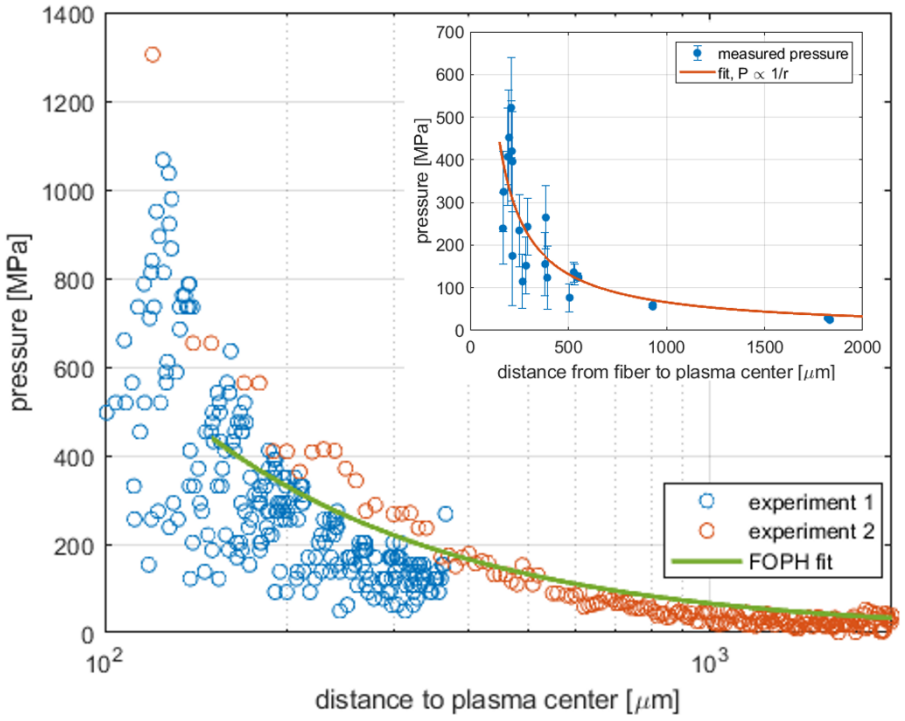

Fig. 9. Shock wave pressures obtained from camera-based shock wave velocity measurements (blue and orange circles), values converted using Eq. (1). The data presented is from both experiments and for all bubble sizes, including the fit on measured pressures from FOPH. Inset: Pressure measurement from FOPH with the corresponding *1/r* best fit.

We find a good agreement of the maximum pressure for both experiments, i.e., the highest laser energies result in very similar pressures for both experiments. Yet, the pressure sensor measurements show consistent values at large distances and systematically lower pressure amplitudes at closer distances. At distances closer than about 250 µm, the consistently lower pressure values differ up to 20 % compared to the imaged-based method. This may be a combined consequence of the used equation of state, and measurement variations due to non-ideal FOPH tip positioning, excitation laser energy instabilities, plasma size, and plasma shape variations. The multi-illumination multi-frame camera-based shock wave velocity measurements allow for up to 18 data points to be extracted from the same LIB event (in Experiment 2, due to the combination

Optics EXPRESS

of a large field of view and burst illumination), but only one pressure trace is obtained per LIB event.

4. Conclusion

This work presents result on plasma shock wave pressure and velocity measurements, combining two all-optical measurement techniques. A fully contactless technique of multi-frame multi-exposure imaging based on bursts of short illumination pulses is used for precise shock wave velocity measurements within a single camera frame. The frame rates are limited to up to 10 MHz by current state-of-the-art high-speed cameras, while the illumination pulses can be emitted at up to 200 MHz repetition rates. The illumination system was coupled to two camera models, obtaining clear images that allowed the measurement of the shock wave velocity. This measured shock wave velocity was converted through the equation of state from Rice & Walsh [22] into pressure. Shock wave pressures and velocities were fully independently measured using the FOPH, providing both shock wave pressure data and shock wave TOF data for comparison and evaluation of the imaging-based method. The obtained shock wave pressures at sub-100 µm distances from the plasma center exceed 500 MPa as measured by the FOPH, while pressures calculated from shock wave velocities exceed 1 GPa. Overall, a good agreement is found, yet for pressures above 400 MPa the equation of state conversion yields higher pressures than measured with the pressure sensor.

We demonstrated nearly jitter-free camera-based shock wave velocity measurements at multiple time delays and in any direction of interest for the same LIB event, due to the illumination system design and synchronization. The measurements are verified and compared with high dynamic range FOPH pressure measurements. The all-optical approach offers the possibility for a wide range of applications in either other high-pressure systems or for event monitoring at frame rates well above the current camera capabilities. While not within scope of this manuscript, we believe that the novel illumination system could be the right tool to probe the equation of state, when embedded with a solid error analysis.

Funding. Deutsche Forschungsgemeinschaft (OH 75/4-1); Javna Agencija za Raziskovalno Dejavnost RS (J2-3057, L2-3171, P2-0270).

Acknowledgments. We thank Specialised Imaging Ltd., UK, for kindly enabling the Kirana 7M camera tests, contributing to an important part of this work.

Disclosures. The authors declare no conflicts of interest.

Data availability. Data underlying the results presented in this paper are not publicly available at this time but may be obtained from the authors upon reasonable request.

References

1. M. H. Niemz, *Laser-Tissue Interactions: Fundamentals and Applications* (Springer-Verlag Berlin Heidelberg, 2007).
2. C. E. Brennen, "Cavitation in medicine," Interface Focus. **5**(5), 20150022 (2015).
3. W. Zapka, W. Ziemlich, and A. C. Tam, "Efficient pulsed laser removal of 0.2 µm sized particles from a solid surface," Appl. Phys. Lett. **58**(20), 2217–2219 (1991).
4. K. M. Kent and E. M. Graber, "Laser Tattoo Removal: A Review," Dermatol. Surg. **38**(1), 1–13 (2012).
5. S. R. Gonzalez-Avila, F. Denner, and C.-D. Ohl, "The acoustic pressure generated by the cavitation bubble expansion and collapse near a rigid wall," Phys. Fluids **33**(3), 032118 (2021).
6. Y. Tian, Y. Li, L. Wang, F. Huang, Y. Lu, J. Guo, and R. Zheng, "Laser-induced plasma in water at high pressures up to 40 MPa: A time-resolved study," Opt. Express **28**(12), 18122 (2020).
7. K. Nahen and A. Vogel, "Plasma formation in water by picosecond and nanosecond Nd:YAG laser pulses. II. Transmission, scattering, and reflection," IEEE J. Sel. Top. Quantum Electron. **2**(4), 861–871 (1996).
8. A. Vogel, I. Apitz, and V. Venugopalan, "Phase transitions, material ejection, and plume dynamics in pulsed laser ablation of soft biological tissues," in *Oscillations, Waves, and Interactions*, T. Kurz, U. Parlitz, and U. Kaatze, eds. (2007).
9. R. A. Van Gorder, "Dynamics of the Rayleigh–Plesset equation modelling a gas-filled bubble immersed in an incompressible fluid," J. Fluid Mech. **807**, 478–508 (2016).
10. P. Harris and H. N. Presles, "Reflectivity of a 5.8 kbar shock front in water," J. Chem. Phys. **74**(12), 6864–6866 (1981).

Optics EXPRESS

11. A. G. Doukas, A. D. Zweig, J. K. Frisoli, R. Birngruber, and T. F. Deutsch, "Non-invasive determination of shock wave pressure generated by optical breakdown," Appl. Phys. B **53**(4), 237–245 (1991).
12. A. Vogel, S. Busch, and U. Parlitz, "Shock wave emission and cavitation bubble generation by picosecond and nanosecond optical breakdown in water," J. Acoust. Soc. Am. **100**(1), 148–165 (1996).
13. S. Geng, Z. Yao, Q. Zhong, Y. Du, R. Xiao, and F. Wang, "Propagation of Shock Wave At the Cavitation Bubble Expansion Stage Induced by a Nanosecond Laser Pulse," J. Fluids Eng. (5), (2021).
14. J. Noack and A. Vogel, "Single-shot spatially resolved characterization of laser-induced shock waves in water," Appl. Opt. **37**(19), 4092–4099 (1998).
15. J. Noack, D. X. Hammer, G. D. Noojin, B. A. Rockwell, and A. Vogel, "Influence of pulse duration on mechanical effects after laser-induced breakdown in water," J. Appl. Phys. **83**(12), 7488–7495 (1998).
16. W. Lauterborn and T. Kurz, "Physics of bubble oscillations," Rep. Prog. Phys. **73**(10), 106501 (2010).
17. T. Shimazaki, S. Ichihara, and Y. Tagawa, "Background oriented schlieren technique with fast Fourier demodulation for measuring large density-gradient fields of fluids," Exp. Therm. Fluid Sci. **134**, 110598 (2022).
18. O. Supponen, D. Obreschkow, P. Kobel, N. Dorsaz, and M. Farhat, "Detailed experiments on weakly deformed cavitation bubbles," Exp. Fluids **60**(2), 33 (2019).
19. K. Hayasaka, Y. Tagawa, T. Liu, and M. Kameda, "Optical-flow-based background-oriented schlieren technique for measuring a laser-induced underwater shock wave," Exp. Fluids **57**(12), 179 (2016).
20. P.-H. Hanzard, T. Godin, S. Idlahcen, C. Rozé, and A. Hideur, "Real-time tracking of single shock waves via amplified time-stretch imaging," Appl. Phys. Lett. **112**(16), 161106 (2018).
21. W. Lauterborn and A. Vogel, "Shock Wave Emission by Laser Generated Bubbles," in *Bubble Dynamics and Shock Waves*, C. F. Delale, ed. (Springer Berlin Heidelberg, 2013), pp. 67–103.
22. M. H. Rice and J. M. Walsh, "Equation of State of Water to 250 Kilobars," J. Chem. Phys. **26**(4), 824–830 (1957).
23. H. Schoeffmann, H. Schmidt-Kloiber, and E. Reichel, "Time-resolved investigations of laser-induced shock waves in water by use of polyvinylidenefluoride hydrophones," J. Appl. Phys. **63**(1), 46–51 (1988).
24. Y. Tagawa, S. Yamamoto, K. Hayasaka, and M. Kameda, "On pressure impulse of a laser-induced underwater shock wave," J. Fluid Mech. **808**, 5–18 (2016).
25. G. Sinibaldi, A. Occhicone, F. Alves Pereira, D. Caprini, L. Marino, F. Michelotti, and C. M. Casciola, "Laser induced cavitation: Plasma generation and breakdown shock wave," Phys. Fluids **31**(10), 103302 (2019).
26. A. Vogel and J. Noack, "Shock-wave energy and acoustic energy dissipation after laser-induced breakdown," in S. L. Jacques, ed. (1998), p. 180.
27. A. A. Aganin and I. N. Mustafin, "Outgoing shock waves at collapse of a cavitation bubble in water," Int. J. Multiphase Flow **144**, 103792 (2021).
28. C. Lechner, M. Koch, W. Lauterborn, and R. Mettin, "Pressure and tension waves from bubble collapse near a solid boundary: A numerical approach," J. Acoust. Soc. Am. **142**(6), 3649–3659 (2017).
29. J. Petelin, Z. Lokar, D. Horvat, and R. Petkovsek, "Localized Measurement of a Sub-Nanosecond Shockwave Pressure Rise Time," IEEE Trans. Ultrason., Ferroelect., Freq. Contr. **69**(1), 369–376 (2022).
30. V. Agrež, T. Požar, and R. Petkovšek, "High-speed photography of shock waves with an adaptive illumination," Opt. Lett. **45**(6), 1547–1550 (2020).
31. D. Han, R. Yuan, X. Jiang, S. Geng, Q. Zhong, Y. Zhang, Z. Yao, and F. Wang, "Nanosecond resolution photography system for laser-induced cavitation based on PIV dual-head laser and industrial camera," Ultrason. Sonochem. **78**, 105733 (2021).
32. E. W. Lemmon, I. H. Bell, M. L. Huber, and M. O. McLinden, *Thermophysical Properties of Fluid Systems*, NIST Standard Reference Database Number 69, NIST Chemistry WebBook (National Institute of Standards and Technology, n.d.).
33. P. Schiebener, J. Straub, J. M. H. Levelt Sengers, and J. S. Gallagher, "Refractive index of water and steam as function of wavelength, temperature and density," J. Phys. Chem. Ref. Data **19**(3), 677–717 (1990).
34. X.-X. Liang, N. Linz, S. Freidank, G. Paltauf, and A. Vogel, "Comprehensive analysis of spherical bubble oscillations and shock wave emission in laser-induced cavitation," J. Fluid Mech. **940**, A5 (2022).
35. R. Pecha and B. Gompf, "Microimplosions: Cavitation Collapse and Shock Wave Emission on a Nanosecond Time Scale," Phys. Rev. Lett. **84**(6), 1328–1330 (2000).
36. E. Faraggi, B. S. Gerstman, and J. Sun, "Biophysical effects of pulsed lasers in the retina and other tissues containing strongly absorbing particles: shock wave and explosive bubble generation," J. Biomed. Opt. **10**(6), 064029 (2005).
37. F. Magaletti, L. Marino, and C. M. Casciola, "Shock Wave Formation in the Collapse of a Vapor Nanobubble," Phys. Rev. Lett. **114**(6), 064501 (2015).